Journal of Power Sources 243 (2013) 682–690

Contents lists available at SciVerse ScienceDirect

Journal of Power Sources

journal homepage: www.elsevier.com/locate/jpowsour

# NMR monitoring of electrode/electrolyte interphase in the case of air-exposed and carbon coated $LiFePO_4$

M. Cuisinier [a], N. Dupré [a,b,*], P. Moreau [a,b], D. Guyomard [a,b]

[a] Institut des Matériaux Jean Rouxel (IMN), CNRS UMR 6502, Université de Nantes, 2 rue de la Houssinière, BP 32229, 44322 Nantes cedex 3, France
[b] Réseau sur le Stockage Electrochimique de l'Energie (RS2E), FR CNRS 3459, France

## HIGHLIGHTS

- Quantitative $^{7}Li$, $^{1}H$ and $^{19}F$ NMR allow describing the interphase structure.
- Electrochemical performance is explained by electrode/electrolyte interaction.
- For air-aged $LiFePO_4$, failure mechanism is driven by dissolution of active material.
- Carbon coating prevents air-aging but leads to organic lithiated species accumulation.

## ARTICLE INFO

*Article history:*
Received 5 April 2013
Received in revised form
27 May 2013
Accepted 3 June 2013
Available online 19 June 2013

*Keywords:*
Lithium batteries
Positive electrode
Interface
MAS NMR

## ABSTRACT

Degradation of the electrochemical performance of $LiFePO_4$ upon air exposure, assigned to a corrosion-type aging mechanism, implies the incorporation of hydroxyl groups and the formation of an amorphous tavorite-like phase at the surface. Using a carbon coating provides an efficient protection from this detrimental process but also modifies the surface in contact with the electrolyte. The formation and evolution of electrode/electrolyte interphases forming on both air-aged and carbon coated $LiFePO_4$ are discussed based on combined quantitative $^{7}Li$, $^{19}F$ MAS NMR, EIS and EELS measurements. Concerning the air-aged $LiFePO_4$, the electrode/electrolyte interactions are dominated by the dissolution of the active material and an exacerbated reaction of incorporated hydroxyl groups with the electrolyte salt, resulting in a LiF rich interphase. This dissolution of the outer part of active material particles is accompanied by the departure of the previously formed interphase and a new interphase is then formed on a newly exposed surface. The resistive LiF rich interphase passivates the active material particles during cycling, forming a resistive film, hindering both Li ion transfer and material corrosion. Cellulose acetate based carbon coating prevents air-aging but yields to an accumulation of organic lithiated species, allowing Li transfer and maintaining good electrochemical performance.

© 2013 Elsevier B.V. All rights reserved.

## 1. Introduction

In the field of lithium battery research, $LiFePO_4$ has attracted considerable attention since it was proposed by Padhi et al. [1] as an alternative to cobalt-oxide based cathode. In particular, its potential use in large scale application such as hybrid electric vehicles (HEV) or electric vehicles (EV) led to a tremendous activity aiming at reducing the particles size [2–5] and/or providing an efficient carbon coating [6–9] in order to overcome the extremely low electronic conductivity of $LiFePO_4$. Such sub-micronic or nanometric particles allow enhancing efficiently the electrochemical performance and reaching theoretical capacity of 170 mAh $g^{-1}$ with high power capability [5,10–12]. On the other hand, the dramatic increase of the surface/volume ratio is proven to induce an important contribution of surfaces and interfaces to the chemistry of the whole battery and can possibly aggravate side or parasitic reactions, detrimental to the electrochemical performance [13–20].

Very few studies deal with surface chemistry [21,22] or interphase evolution of $LiFePO_4$ electrode material [23–25] upon its storage in ambient atmosphere or its operation in a lithium battery as it was considered as chemically inert. From the structural and electrochemical characterization of air-aged materials, reaction mechanisms for the aging process of $LiFePO_4$ were proposed in previous works [26–29]. The aging process of $LiFePO_4$ upon atmosphere exposure has been exhaustively described and the

* Corresponding author. Institut des Matériaux Jean Rouxel (IMN), CNRS UMR 6502, Université de Nantes, 2 rue de la Houssinière, BP 32229, 44322 Nantes cedex 3, France. Tel.: +33 (0)2 40 37 63 29.
*E-mail address:* nicolas.dupre@cnrs-imn.fr (N. Dupré).

0378-7753/$ – see front matter © 2013 Elsevier B.V. All rights reserved.
http://dx.doi.org/10.1016/j.jpowsour.2013.06.042

presence of Fe(III) localized at the particles surface has been assigned to a $LiFePO_4(OH)$ amorphous hydrated ferric phosphate formed through a corrosion-type reaction, causing the degradation of the electrochemical performance. The experimental conditions of formation, growth and modification of the interphase are still ambiguous, especially as they may be influenced by surface modification of the active material after storage or aging.

In this work, the impact of such aging on the interphasial chemistry is investigated and discussed. The degradation of the electrochemical performance of $LiFePO_4$ upon air exposure being assigned to a corrosion-type aging mechanism, implying both atmospheric oxygen and moisture, a trivial protection from this detrimental reaction is also considered here through the use of a carbon coating. Not only is the presence of a conducting carbon layer expected to improve the electrical properties of the material but carbon being hydrophobic, it is also aimed at impeding the chemisorption and incorporation of hydroxyl group in the underlying $LiFePO_4$ surface leading to $LiFePO_4(OH)$ formation. The formation and evolution of interphases that form on both air-aged and carbon coated $LiFePO_4$ are then followed and discussed in the light of combined quantitative $^7$Li, $^{19}$F MAS NMR, EIS and EELS measurements. Therefore, we aim here at monitoring the electrode/electrolyte interface in the cases of air-aged $LiFePO_4$ and carbon-coated $LiFePO_4$. The evolution of their modified surfaces, degraded with the incorporation of hydroxyl groups or protected with a carbon layer, is compared with the evolution of the interphase of a Pristine $LiFePO_4$.

Our results illustrate the possibility to correlate the nature and evolution of the $LiFePO_4$/electrolyte interphase, as probed by NMR spectroscopy, to the material surface chemistry, and finally elucidate the overall electrochemical performance evolution. In the case of the air-aged $LiFePO_4$, we show that the electrode/electrolyte interactions are dominated by the dissolution of the active material and an exacerbated reaction of incorporated hydroxyl groups with the electrolyte salt, resulting in a LiF rich interphase. This dissolution of the outer part of active material particles seems to be accompanied by the departure of the previously formed interphase and a new interphase is then formed on a newly exposed surface. The resistive LiF rich interphase seems to passivate the active material particles during cycling, forming a resistive film and hindering both Li ion transfer and material corrosion. On the other hand, we show that cellulose acetate based carbon coating prevents air-aging but also leads to an accumulation of organic lithiated species, allowing Li transfer and maintaining good electrochemical performance.

## 2. Experimental

The $LiFePO_4$ material was synthesized via the solid-state method developed by Yamada et al. and described in previous work [2,27,28,30]. Stoichiometric amounts of precursors, namely lithium carbonate $Li_2CO_3$, iron acetate $FeC_2O_4 \cdot 2H_2O$, and diammonium hydrogenophosphate $(NH_4)_2HPO_4$, are first ball milled in acetone at 240 rpm for 6 h. The annealing is then carried out at 700 °C for 6 h under $Ar/H_2$ atmosphere, after setting a careful vacuum of the furnace to avoid iron oxidation. The iron acetate precursor used in the synthesis is responsible for the presence of carbon residues accounting for approx. 1 wt% and after annealing at 700 °C under $Ar/H_2$ atmosphere, olivine particles size has been evaluated to 120 nm. The pristine bare sample is here referred as B-P.

In order to evaluate the protection offered by surface modification, a carbon coating was deposited afterward. Two sources of carbon, namely sucrose and cellulose acetate have been used in this work, leading to an overall carbon content of 4 wt% [6]. Post annealing is performed at 700 °C for 3 h under $Ar/H_2$ atmosphere. Sucrose-derived and cellulose acetate-derived carbon-coated samples are labeled S-P and CA-P, respectively.

Air-aging was carried out at 120 °C for 30 days under ambient atmosphere, and the resulting samples, from bare and C-coated materials, are referred as B-A, S-A and CA-A, respectively.

The XRD diffractograms were obtained on a D5000 ADVANCE (BRUKER AXS) apparatus using $CuK_\alpha$ radiation over the [15–90°] $2\theta$ range and TOPAS software was used for Rietveld refinements. For amorphous phase quantification, the samples were thoroughly mixed with 35% of reference $TiO_2$ anatase powder (particle size of 50 nm) and Brindley correction [31] was taken into account.

The $^{57}$Fe Mössbauer spectra were collected with a $^{57}$Co $\gamma$-ray source. Velocity and isomer shift calibration were performed using $\alpha$-Fe as a standard at room temperature.

Electrochemical studies were carried out on a Biologic MPG2 using Swagelok-type cells. Electrodes were constituted of 80 wt% of active material, 10 wt% of carbon (ketjenblack in addition to the possible coating) and 10 wt% carboxymethylcellulose (CMC). In order to get rid of the binder contributions on $^1$H MAS NMR and XPS spectra, a binder-free formulation (active material: ketjenblack carbon weight ratio as 90:10) was also used. For both CMC-based electrodes and binder-free electrodes, slurries made with water were deposited on 1 $cm^2$ aluminum disks and then dried under vacuum at 100 °C for 24 h. The negative electrode was made of a disk of lithium metal.

Electrochemical impedance spectroscopy (EIS) measurements (from 10 mHz to 200 kHz) were obtained using a VMP/Z apparatus (Bio-logic, France). A home-made Swagelok-type three electrodes cell was used. The negative electrode was made of a disk of lithium metal. The reference electrode consists of a ring of lithium metal surrounding the working electrode. Measurements have been performed at the end of a 5 h relaxation rest upon discharge down to 2.5 V and upon charge up to 4.5 V for different C/10 galvanostatic cycles at ambient temperature.

X-ray photoelectron spectroscopy (XPS) data have been collected after different cycle numbers using a Kratos Ultra Axis spectrometer. The X-ray source is AlK working at 1253.6 eV and the spot size is $0.7 \times 0.3$ mm. A special air-tight sample holder has been used to transfer the samples from the glove box to the spectrometer, in order to avoid any reaction with ambient atmosphere. Semiquantitative XPS analysis has been performed using pseudo-Voigt function constrained by full width at half-maximum (FWHM) ranges typical of each element. The validity of the analyses was confirmed by an experimental M/O ratio close to the theoretical one for the bare pristine compound. Binding energies were fixed at $0.2 \pm$ eV of the given value.

$^7$Li and $^{19}$F NMR experiments were carried out at room temperature on a Bruker Avance-500 spectrometer ($B_0 = 11.8$ T, Larmor frequencies $\nu_0$ ($^7$Li) = 194 MHz, $\nu_0$ ($^{19}$F) = 470 MHz). MAS spectra were obtained by using a Bruker MAS probe with a cylindrical 2.5 mm o.d. zirconia rotor. Spinning frequencies up to 29 kHz were utilized. $^7$Li NMR spectra were acquired by making use of a single pulse sequence coupled with a pre-acquisition time of 4.5 μs allowing the separation of the surface lithium signal from the bulk signal. By this mean, only diamagnetic species on the surface of the paramagnetic active material were observed [32–34]. $^{19}$F NMR spectra were acquired using a Hahn echo sequence to discard the significant contribution from the probe signal. All spectra displayed in this work were normalized taking into account the number of scans, the received gain, and the mass of sample. $^7$Li and $^{19}$F integrated intensities were determined by using spectral simulation (Dmfit software [35]). $T_{2r}$ were estimated from the isotropic resonance linewidths [25,36,37].

EELS analyses were performed on a Hitachi HF 2000 (Field Emission Gun, 100 KV) with a probe diameter of 20 nm. In order to minimize carbon contamination and irradiation damage, samples were cooled down at liquid nitrogen temperature. Spectra were recorded on a modified Gatan 666 parallel spectrometer equipped with a CCD camera and a Digipeels command. The energy resolution was 1.8 eV (given by the zero loss peak (ZLP) full width at half maximum) with a dispersion of 0.3 eV/pixel. Convergence and collection angles were respectively of 1.4 and 18.2 mrad. All recordings were dark count and gain corrected and then processed using standard tools provided for quantification in Digital Micrograph. Samples were probed using TEM in order to ensure the representative character of the particles chosen for EELS analysis.

## 3. Results

### 3.1. Pristine materials characterization

The experimental XRD patterns obtained for as-synthesized bare $LiFePO_4$ (B–P), carbon-coated $LiFePO_4$ obtained from cellulose acetate (CA-P) and carbon-coated $LiFePO_4$ obtained from sucrose (S-P) were in agreement with pure $LiFePO_4$ (see Supporting information, Fig. S-1). In each case, the diffraction peaks are in full agreement with the $LiFePO_4$ olivine structure indexed in the orthorhombic *Pnma* space group and no evidence of impurity phases could be observed. Cell volumes inferior to 291.5 $Å^3$ (see Supporting information, Table S-1) suggest no significant Li/Fe exchange between the 4a and 4c sites [38].

Additional Mössbauer spectroscopy on pristine materials (see Supporting information) indicated only a 3–5% Fe(III) content that can be assigned to a highly disordered octahedral phosphate environment close to that of Fe(III) in mineral olivine [39] and can be a sign of a defective or amorphous ferric phase [40], which presence seems unavoidable unless taking drastic storage and handling precautions [41,42].

The powder morphologies of the products are shown in Fig. 1. All samples display aggregates (5–20 μm) of small grains of approximately 100–200 nm. The carbon coating being realized after the material synthesis, the 4 wt% of carbon are found on the surface of the aggregates rather than that of the primary particles. Specific surface area measurements by the BET method give 22 $m^2 g^{-1}$, 19 $m^2 g^{-1}$ and 25 $m^2 g^{-1}$, for samples B-P, S-P and CA-P, respectively. In addition, 100–200 nm particle size estimated from coherence domain lengths (Table S-1) are confirmed by SEM (Fig. 1).

TEM also highlights the distribution of carbon in the different samples and high-resolution images are displayed in Fig. 2. Both coated materials exhibit at least a 2 nm-thick carbon layer that covers the whole surface, even if thicker deposits are also found within the aggregates. No bare $LiFePO_4$ surface has been observed during these experiments.

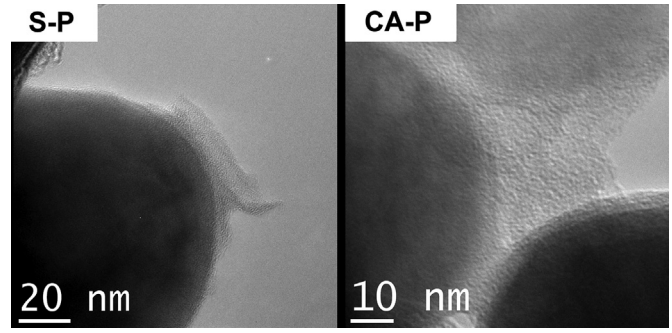


**Fig. 2.** Transmission electronic micrographs detailing carbon distribution in S-P and CA-P.

From this first series of characterization, it can be inferred that the coating has not modified the active material. In order to further characterize the carbon coating, and possibly differentiate samples S/LFP and CA/LFP, EELS analyses were performed both on free surfaces (S-1 and CA-1 spectra on Fig. 3) and aggregate interstitial spaces filled by carbon (S-2 and CA-2 spectra on Fig. 3). Characteristic C-K edges observed on these two samples are displayed in Fig. 3. A careful analysis of the C-K edge, as summarized hereunder in Table 1, can provide valuable information regarding the hybridization of carbon in the coating, indicating its conducting properties. Hence the presence of a sharp $\pi^*$ peak at 285 eV suggests a main $sp^2$ hybridization for carbon in the two coatings. The width of this peak indicates the degree of crystallinity and the $sp^2/sp^3$ ratio can be deduced by comparing the intensity of the $\pi^*$ peak with the rest of the spectrum ($\pi + \sigma$), taking graphite as the reference for

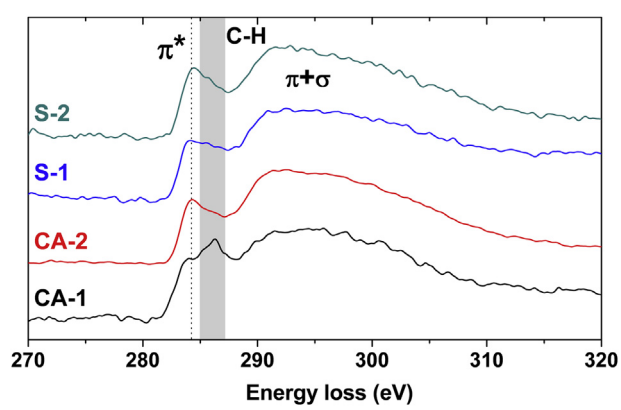


**Fig. 3.** EELS C-K edges measured at the surface (1) and in the interstitial space (2) for S-P (noted S-1 and S-2) and CA-P (noted CA-1 and CA-2). The gray band highlights the presence of C–H and C=O bands in the $\pi^*$ domain.

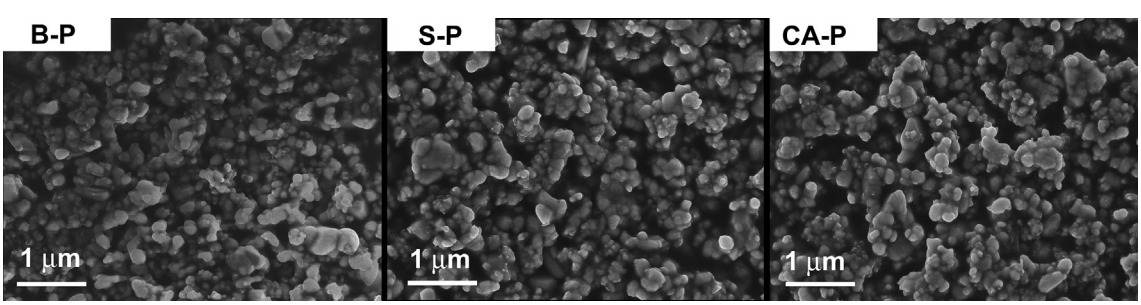


**Fig. 1.** SEM pictures of B-P, S-P and CA-P.

**Table 1**
Results of averaged C-K edge EELS analyses on the coating of S-P and CA-P.

| | | $\pi^*$ Peak width (eV) | $R = \pi^*/(\pi + \sigma)$ intensity % | % $sp^2$ |
|---|---|---|---|---|
| S-P | Surface C | 2.4 (4) | 9.6 (15) | 74 (10) |
| | Interstitial C | 2.8 (4) | 10.7 (12) | 81 (7) |
| CA-P | Surface C | 2.7 (2) | 11.6 (4) | 87 (3) |
| | Interstitial C | 2.7 (3) | 11.7 (3) | 87 (2) |
| Graphite | | 1.8 (1) | 14.0 (1) | 100 |

pure $sp^2$ hybridization [43–46]. As observed on the spectra labeled CA-1 and S-1, additional intensity is sometimes detected between the $\pi^*$ and the $\pi + \sigma$, either as a distinct peak or a shoulder around 286 eV. This spectral feature is assigned in the literature to the presence of C–H and C=O bands [47], and indicates an incomplete carbonization of the organic precursor during the post annealing, detrimental to the electronic conductivity.

Based on punctual EELS analyses averaged in Table 1, it appears that the carbon referred as S-P and CA-P exhibits roughly similar crystallinity and $sp^2/sp^3$ ratio. However, data gathered on S-P sample show a significantly broader dispersion, and average values differ between the thin layer present at the particles surface and in the interstitial space. These observations suggest a more pronounced inhomogeneity of the C coating at the nanoscale level for this sample.

### 3.2. Aged material characterization – carbon coating protection

Fig. 4 exhibits the XRD patterns obtained for the samples having undergone subsequent air-aging for one-month (B-A, S-A and CA-A). In each case, the observed diffraction peaks are in full agreement with the $LiFePO_4$ olivine structure indexed in the orthorhombic *Pnma* space group and no evidence of crystallized impurity phases could be observed. The results of Rietveld refinements for the three samples mixed with $TiO_2$ are given in Table 2, including the amorphous content arising from the carbon coating or the air-aging, as discussed in Ref. [29].

In previous works [26–29], we exhaustively described the aging process of $LiFePO_4$ upon atmosphere exposure, and assigned the presence of Fe(III) localized at the particles surface to amorphous hydrated ferric phosphates formed through a corrosion-type

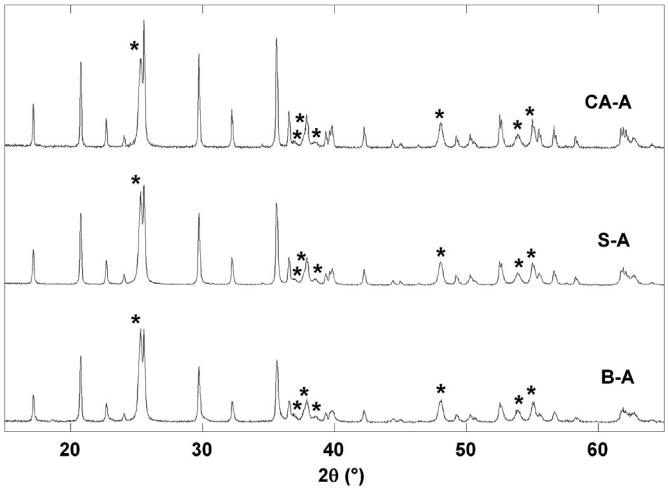


**Fig. 4.** XRD patterns of air-aged bare and carbon-coated $LiFePO_4$: B-A, S-A and CA-A. Patterns have been normalized with respect to the $TiO_2$ intensity. $TiO_2$ anatase reflections are marked by an asterisk.

**Table 2**
Lattice parameters and selected results from the Rietveld refinement of $LiFePO_4$–$TiO_2$ mixtures displayed in Fig. 4. The 4% of amorphous carbon due to the coating for the two-coated sample have been subtracted (see Supporting information).

| | | B-A | S-A | CA-A |
|---|---|---|---|---|
| *R*-values | $R_{wp}$ (%) | 9.47 | 10.14 | 9.05 |
| | $R_{Bragg}$ (%) | 2.984 | 2.923 | 3.175 |
| Cell volume (Å$^3$) | | 291.339(6) | 291.340(7) | 291.339(9) |
| Crystallite size (nm) | | 96.8(6) | 103.2(4) | 101.3(3) |
| Lattice parameters | *a* (Å) | 10.3302(3) | 10.3303(5) | 10.3304(4) |
| | *b* (Å) | 6.0085(8) | 6.0083(2) | 6.0088(4) |
| | *c* (Å) | 4.6941(6) | 4.6949(1) | 4.6934(2) |
| Fe on Li 4a site (%) | | 0.9(1) | 0.8(1) | 0.8(1) |
| Amorphous phase(s) (%) | | 23 | 19 | 6 |

reaction. The protection offered by a carbon coating is evaluated here via a simple comparative aging test between the pristine material and the samples prepared from the carbonization of sucrose or cellulose acetate. Mössbauer measurements shown in Fig. 5 (left) highlight the oxidation of bare $LiFePO_4$ upon air-aging (from 4% of Fe(III) in sample B-P to 21% in sample B-A). The carbon coating formed from carbonization of acetate cellulose seems to protect efficiently the active material from surface corrosion as the spectrum of CA-A only exhibits 6% of Fe(III) after similar aging treatment. On the other side, the increase from 3% (in S-P) to 18% Fe(III) observed in the case of the carbon coated $LiFePO_4$ using sucrose as precursor, indicates that such coating seems to be inefficient toward the air-aging process.

The electrochemical performance of all $LiFePO_4$ samples were evaluated and the corresponding specific discharge capacities obtained at a C/10 regime are displayed in Fig. 5 (right). The specific capacities observed for the carbon-coated materials (S-P and CA-P) are close to published values, although slightly lower (160 mAh $g^{-1}$), as the electrode formulation was not optimized. As expected, the non carbon-coated material (B-P) exhibit both lower performance and lower capacity retention (−6% after 100 cycles) due to the absence of conductive/protective carbon, in agreement with published data [2,6]. Concerning aged samples, it appears clearly that the initial capacity of the bare material (145 mAh $g^{-1}$ for sample B-A) cannot be maintained over more than few cycles and fades rapidly (−30% after 20 cycles, −50% after 100 cycles). On the contrary, even after air-aging, coated $LiFePO_4$ CA-A can still deliver a fair discharge capacity (155 mAh $g^{-1}$ after 100 cycles) which confirms the effective protection offered by the carbon layer toward the detrimental effects of air-aging. In spite of its experimental demonstration, the protection mechanism of the carbon layer remains unclear. In fact, the other carbon coating envisaged, prepared from sucrose precursor (S-A) is confirmed to be almost

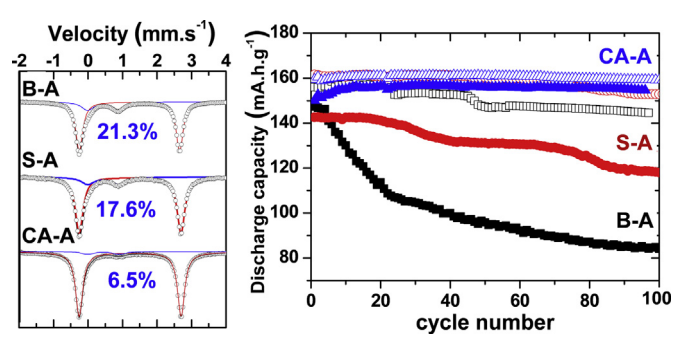


**Fig. 5.** Left, Mössbauer spectra of one month aged B-A, S-A and CA-A. Right, discharge capacity at C/20 rate of bare and coated LFP samples before (open symbols) and after (closed symbols, B-A, S-A and CA-A) one month aging at 120 °C.

ineffective toward air induced $LiFePO_4$ oxidation. EELS analysis (Fig. 3 and Table 1) carried out on pristine coated materials highlighted an important carbonization inhomogeneity for S-P. The implied presence of residual polar domains at the particles surface would favor water adsorption rather than repel it. On the contrary, organic residues are well distributed in the carbon layer present in CA-P, forming a barrier sufficiently hydrophobic. Then, the difference in the hydrophobic properties of the two coatings may explain such different reactivity. These results emphasize the decorrelated electronic and protective properties of the carbon coating. As a matter of fact, even if the carbon coating covers the whole surface of active material, leading to the access to high specific capacity and capacity retention at high regime, it does not necessary protect the material from the degradation due to air-aging. The carbon coating based on sucrose precursor being ineffective, it will not be investigated further in the present study.

### 3.3. Effect of air aging on the reactivity toward electrolyte – interphase evolution for air-aged $LiFePO_4$

At this point, it is not clear whether the poor electrochemical performance of the air-aged sample can be explained by iron dissolution, growth of an insulating interphase and/or loss of electrical contact within the electrode. In the case of pristine $LiFePO_4$ upon storage in $LiPF_6$ based electrolytes, Koltypin et al. observed a decrease of the performance along an increase of the electrode resistance that they attributed to Fe dissolution at elevated temperature [16]. ICP measurements carried out after a one month long soaking experiment at 55 °C demonstrated a three times more important dissolution with 1.4 g(Fe) $L^{-1}$ in the case of the air-aged B-A compared to the pristine B-P (0.5 g(Fe) $L^{-1}$) while room temperature storage resulted for both samples in lesser olivine dissolution (~0.04 g(Fe) $L^{-1}$). Thus, $LiFePO_4$ reactivity toward electrolyte is found exacerbated by prior air exposure, especially at higher temperature. The role of hydroxyl groups chemisorbed or incorporated in the bulk surface (susceptible to react with $LiPF_6$ to form highly corrosive HF) should be decisive in the interphasial chemistry, in particular on the formation and/or evolution of the interphase between the active material and the electrolyte. Such an interphase, able to influence strongly the electrochemical performance of the material is investigated in the following.

EIS experiments performed on air-aged sample (B-A) over 20 galvanostatic cycles (Fig. 6) show severe differences with the impedance stability typically observed for pristine $LiFePO_4$ [25] for which no significant evolution could be observed during the 20 cycles under investigation. The frequency characterizing the flat pseudo capacitance associated with charge transfer resistance and the solid polymer layer (SPL) [48] significantly decreases along cycling, while its resistance increases from 15 to 40 Ω (20–60 Ω) at the end of charge (discharge) between the first and 20th cycles. This observation implies a progressive surface blocking for the air-aged B-A sample. Moreover, the appearance of a high frequency semi-circle after the 20th discharge indicates that the interphase then acts truly as a continuous resistive film. This additional high frequency loop, not observed for B-P sample [25], remains visible on the subsequent cycles. The impedance, then stabilized, suggests an effective passivation of the electrode surface at this stage. Noteworthy, this stabilization of the interphase might allow explaining the break observed in the fading of the specific capacity of sample B-A in Fig. 5.

The surface reactivity toward electrolyte has been investigated by NMR and Fig. 7 shows the $^7$Li NMR spectra measured at the end of the 1st, 5th and 20th charges and discharges for B-A. Previous results concerning the behavior of pristine $LiFePO_4$ (sample B-P) [25] are summarized on Fig. 8, including $^7$Li and $^{19}$F quantitative NMR data.

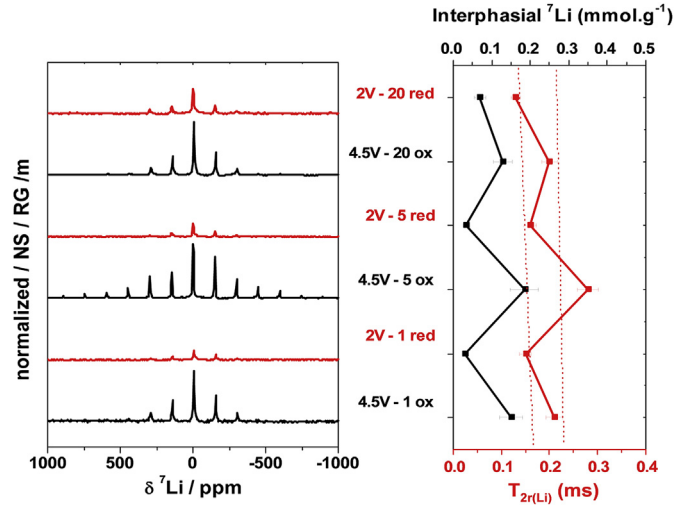


**Fig. 7.** Normalized $^7$Li NMR spectra for air-aged $LiFePO_4$ sample (B-A) at the end of the 1st, 5th and 20th charges and discharges at a C/20 rate in $LiPF_6$ EC:DMC (left). Amounts of interphasial lithium deduced from integrated intensities, as well as $T_{2r}$ estimated from the signal width (right).

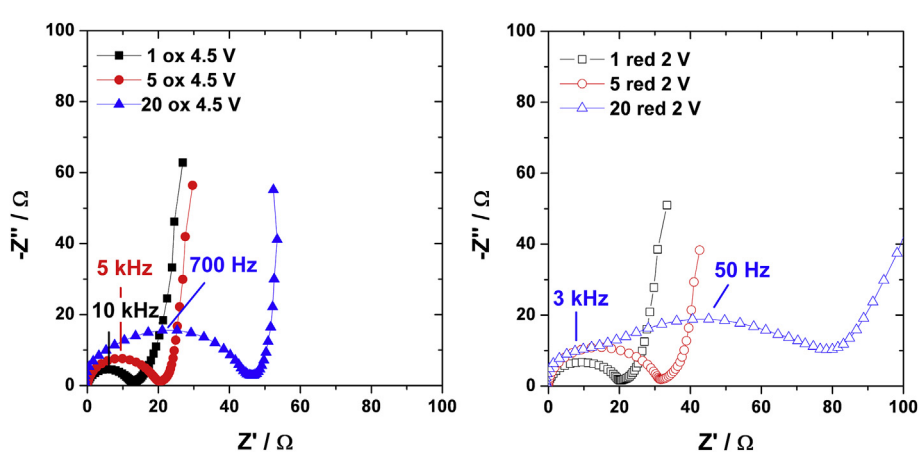


**Fig. 6.** Nyquist plots of EIS performed on air aged B-A at the end of the 1st, 5th and 20th charges (closed symbols, left) and discharges (open symbols, right) at a C/20 rate. N.B. For this particular experiment, impedance stabilization is observed at the 18th cycle (±2 cycles when repeating experiments).

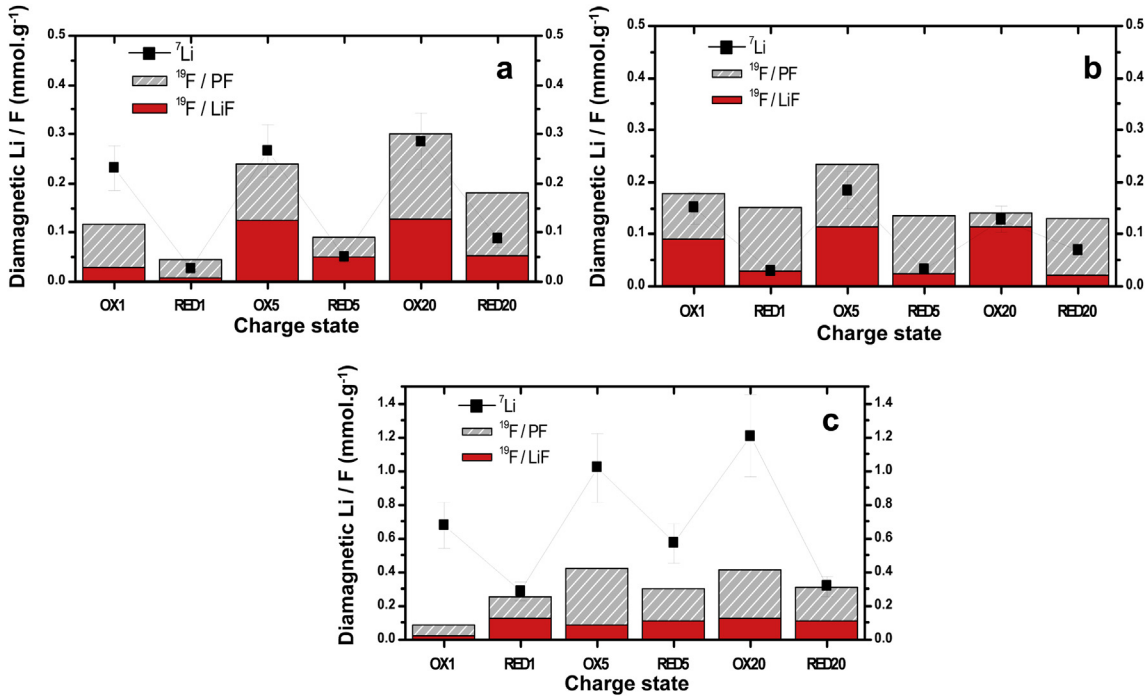


**Fig. 8.** Evolution of the amounts of lithium, and fluorine (in the form LiF and fluorophosphates) contained in interphasial species on B-P (a), B-A (b) and CA-P $LiFePO_4$ (c) along the 20 first electrochemical cycles.

The potential dependency (end of charge vs. end of discharge) observed for the amount of interphasial lithium on B-P and B-A (Figs. 7, 8(a) and (b)) is retained. In addition, no lithiated product accumulation occurs at the electrode surface along the electrochemical cycling, compared to B-P sample. As shown in previous work [25], the evolution of residual $T_{2r}$, allows monitoring the interaction between interphasial lithiated species and the paramagnetic active material through the distance dependent electron-nucleus dipolar interaction [31,32,49]. In the case of B-P [25], the increase of $T_{2r}$ when cycling was correlated with the progressive stacking of additional interphasial species further away from the surface of active material, resulting in a weaker overall electron-nucleus dipolar interaction [25]. As observed on Fig. 7 (right), $T_{2r}$ estimated for B-A does not lengthen for similar SOC along the cycling. Assuming that the precipitation/dissolution process of the SPL is maintained, the overall interaction between the interphase and the surface of active material is not weakened by repeated cycles for B-A, supporting the absence of accumulation of lithiated species along cycling.

The evolution of fluorinated compounds on the surface of B-A (Fig. 8(b)) follows that of lithiated species. Rather than an overall accumulation of interphasial species between the first and 20th cycle that would explain the growth of a resistive film as observed by EIS, $^{7}$Li and $^{19}$F NMR highlight the almost perfect reversibility of the interphase precipitation/dissolution process. No accumulation of lithiated and/or fluorinated species could be observed along the 20 studied cycles.

In this regard, the evolution of the electrode/electrolyte interphase, as probed by NMR and EIS, appears quite different for pristine B-P and air-aged B-A material. Compared to the SPL model considered at the surface of pristine B-P, the interphase observed on air-aged B-A contains a significantly higher ratio in salt decomposition products such as LiF and fluorophosphates. In particular, attention should be paid to the amount of Li in LiF in the oxidized state, accounting for 50–90% of the total detected interphasial lithium, while the high voltage SPL on B-P only contains 20–50% of lithium under the form of lithium fluoride. Hence, the interphase of B-A can be seen as a mixture of highly resistive LiF and nonlithiated fluorophosphates or nonlithiated polymeric species [25,50–55], these latter being invisible to the present NMR experiments but detected by XPS in a previous publication by our group [25]. The higher ratio of resistive species in that case is consistent with formation of a resistive film observed by EIS during the electrochemical cycling. Although the overall amount of LiF does not seem to change significantly from one cycle to another, the appearance of the second EIS semi-circle suggests a progressive concentration or redistribution of the resistive species such as LiF and nonlithiated species toward a complete covering or passivation of the surface of active material.

Considering the aggravated Fe dissolution observed for the air-aged material, a plausible hypothesis regarding the interphasial processes is that chemisorbed/incorporated water or hydroxyl groups contained in the surface $LiFePO_4(OH)$ phase would favor the dissolution of the electrode material upon contact with the electrolyte or cycling. Indeed, in the case of the air-aged material, the surface in contact with the electrolyte contains a significant amount of OH groups and corrosive HF can be now formed not only from reaction with trace of water in the electrolyte [56–58] but also directly from reaction with the OH rich surface of the active material. The produced HF can subsequently attack the active material, then driving the dissolution of $LiFePO_4$ (or rather of surface $LiFePO_4(OH)$) as represented in Fig. 9. HF can also react with interphasial species, especially lithiated organic or polymeric species, to form (among others) an important amount of highly resistive LiF [59] as follows:

$$HF + ROCO_2Li\ (s) \rightarrow LiF\ (s) + ROCO_2H \quad \text{(Ia)}$$

$$2HF + Li_2CO_3\ (s) \rightarrow 2LiF\ (s) + H_2CO_3 \quad \text{(Ib)}$$

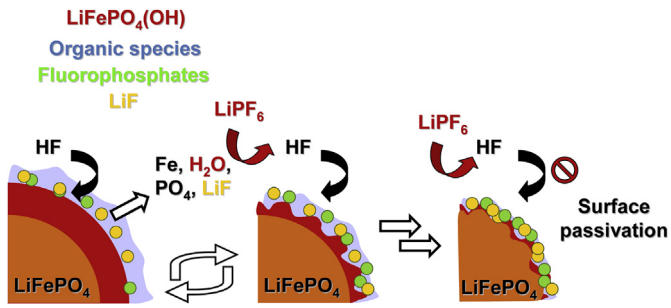


**Fig. 9.** Proposed failure mode of air-aged B-A (exhibiting a $LiFePO_4(OH)$-rich surface) along cycling in conventional $LiPF_6$ 1 M in EC:DMC (1:1) electrolyte. Traces of HF can corrode the surface of the $LiFePO_4(OH)$ rich surface while the SPL is forming (left). Liberated OH radicals (or $H_2O$) are then also free to react with the electrolyte $LiPF_6$ leading to the formation of HF and thus fueling the corrosion process (middle). This process stops or slows down significantly when the surface is passivated with non-porous "inorganic" layer (right).

Most likely, the dissolution of active material, driven by the generation of fluorhydric acid, would be accompanied by the (partial) departure of the interphase previously formed. A new interphase is then most probably forming on a newly exposed surface.

The drastic fading of electrochemical performance of air-aged $LiFePO_4$ material can be therefore considered as the result of reaction of aqueous species chemisorbed/incorporated upon air exposure with $LiPF_6$ to form HF. The degradation of both the active material and the electrolyte would thus last until the full consumption of the aqueous species is reached, or unless a passivation film is formed, which seems to happen here around the 20th cycle. Consequently, electrode surface passivation occurs due/thanks to the presence of a mostly inorganic interphase, containing a significant ratio of resistive LiF as suggested from NMR experiments. This interphase is likely to be denser than the SPL observed on pristine $LiFePO_4$ (B-P), acting as an effective barrier from further acidic attacks.

### 3.4. Effect of carbon coating on the reactivity toward electrolyte

Proven to influence surface reactivity of $LiFePO_4$ against air exposure and to prevent the formation of surface $LiFePO_4(OH)$, the carbon coating obtained from cellulose acetate is also susceptible to modify the reactivity toward electrolyte and therefore to influence the formation and evolution of the electrode/electrolyte interphase.

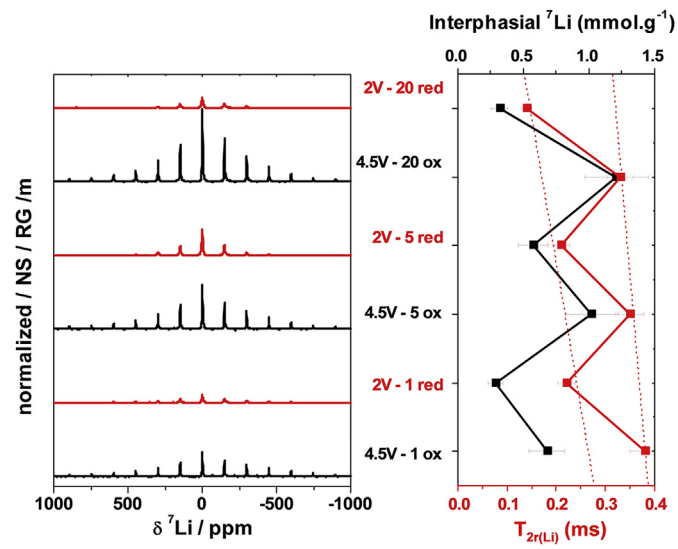


**Fig. 11.** Normalized $^7Li$ NMR spectra for carbon coated $LiFePO_4$ sample (CA-P) at the end of the 1st, 5th and 20th charges and discharges at a C/20 rate in $LiPF_6$ EC:DMC (left). Amounts of interphasial lithium deduced from integrated intensities, as well as $T_{2r}$ estimated from the signal width (right).

In the following, we focus on the study of CA-P and not CA-A since (i) the carbon coating based on cellulose acetate prevents the active material from aging and (ii) the aging of the carbon coating itself in ambient atmosphere is out of the topic of the present paper. Fig. 10 displays the EIS Nyquist plots recorded along the 20 first electrochemical cycles for the CA-P material.

The initial values for CA-P are similar to those measured for B-P (40 Ω and 60 Ω for charged and discharged samples, respectively [25]). Surprisingly however, the impedance of this carbon-coated material shows a significant increase of the semi-circle associated to the charge transfer resistance and double layer capacitance between the first and 20th cycle. Low frequency processes are not affected, and no additional semi-circle indicating the formation of a resistive film can be observed. These results suggest a progressive hindering of the charge transfer and therefore of the intercalation/deintercalation process without the clear formation of a resistive film covering the whole surface of the active material.

The $^7Li$ NMR spectra for the corresponding samples are shown in Fig. 11. Again, the potential dependent precipitation/dissolution process is retained (Fig. 11, left), indicating that such process is not

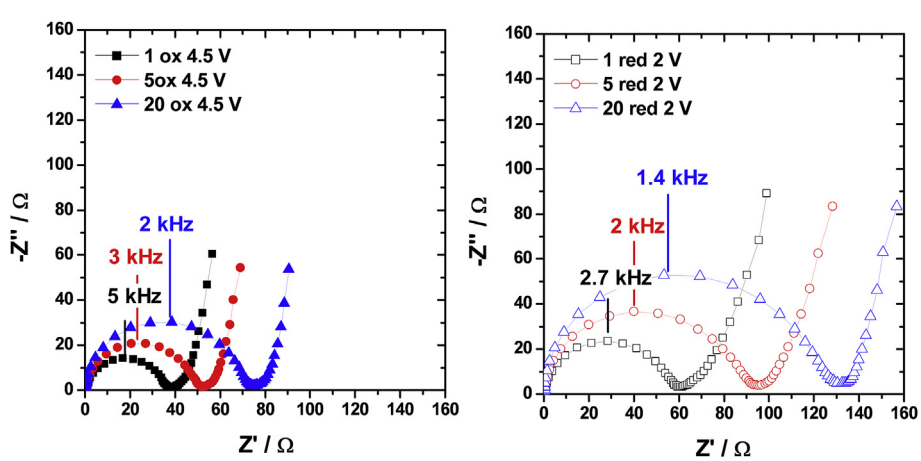


**Fig. 10.** Nyquist plots of EIS performed on CA-P at the end of the 1st, 5th and 20th charges (closed symbols, left) and discharges (open symbols, right) at a C/20 rate.

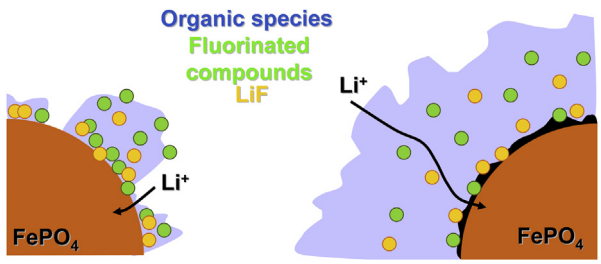


**Fig. 12.** Overview of the impact of a carbon coating on $LiFePO_4$ reactivity toward conventional $LiPF_6$ 1 M in EC:DMC (1:1) electrolyte in the case of CA-P. The presence of a carbon coating (right) leads to a more significant accumulation of lithiated organic species compared to a bare $LiFePO_4$ (left).

influenced by a change in the surface chemistry of the active material whether through air-aging or through carbon coating but rather by the $LiFePO_4/LiPF_6$ (EC:DMC) couple subjected to potential changes. The most striking result is that, not only the amount of interphasial lithium notably increases between the first and 20th charge, but also that the amount of interphasial Li is 4–6 times larger compared to B–P indicating a considerably increased amount of lithiated species on the surface of the composite material. Besides, the gradual decrease of $T_{2r(\mathrm{Li})}$ suggests an increasing intimacy of the interphase with the paramagnetic active material. Compared to bare B–P, the increase of impedance along cycling for the coated material may thus be assigned to a gradual covering of the electrode surface by interphasial species rather than their stacking on the top of each others.

To understand how CA-P material is capable of delivering a constant discharge capacity in spite of the significant increase of charge transfer resistance, complementary $^{19}F$ NMR measurements were carried out. As shown in Fig. 8(c), the accumulation of interphasial lithiated species at the surface of CA-P is not accompanied by a comparable accumulation of fluorinated salt decomposition products.

While the amount of LiF exhibits almost no evolution, the amount of fluorophosphates remains significantly lower than the amount of interphasial lithium. Thus, the SPL covering CA-P at high voltage must be extremely rich in lithium under the form of organic/polymeric species that dissolve during the subsequent discharge rather than insoluble inorganic salts. Although the charge transfer at the interface is affected, lithium can travel through this Li-rich interphase, and therefore no effect on the discharge capacity is observed. An overview of the impact of a carbon coating on $LiFePO_4$ reactivity toward electrolyte is pictured on Fig. 12. The absence of evolution in the amount of LiF suggests that contrary to solvents decomposition, the salt decomposition is not aggravated in the case of CA-P. These combined observations might be explained by the material surface chemistry. In fact, the material surface has been made hydrophobic by the presence of the coating, and a lower amount of adsorbed water impurities is expected for CA-P compared to B-P. Hence, the increase of contact surface with the deposition of the carbon layer (BET specific surface area increases from 21 $m^2\ g^{-1}$ to 25 $m^2\ g^{-1}$) does not necessary favor parasitic reactions with $LiPF_6$. On the contrary, the decomposition of electrolyte solvents is aggravated during charge by the increase of contact surface due to the carbon porosity.

## 4. Conclusions

Although widely considered as inert toward air exposure, $LiFePO_4$ exhibits certain reactivity toward atmospheric oxidizing species, namely oxygen and moisture. The corresponding aging process of $LiFePO_4$ leads to important surface modifications, even at moderate temperature. As a matter of fact, this corrosion-type mechanism leads to the incorporation of hydroxyl groups, under the form of an amorphous $LiFePO_4(OH)$ phase appearing at the surface of $LiFePO_4$ particles. Following this reaction, the presence of aqueous species in the material dramatically modifies the material reactivity toward electrolyte.

In fact, the vulnerability of $LiFePO_4$ against acidic impurities is not only confirmed here, but proves considerably aggravated after air aging. The work conducted here demonstrated that in such a case, the electrode/electrolyte interactions are dominated by the dissolution of the active material and the reaction of incorporated hydroxyl groups with the electrolyte salt. The surface in contact with the electrolyte, containing a significant amount of OH groups, corrosive HF is formed not only from reaction with trace of water in the electrolyte but also directly from reaction with the OH rich surface of the active material. Most likely, this dissolution of the outer part of active material particles is accompanied by the departure of the previously formed interphase and a new interphase forms on a newly exposed surface. The exacerbated degradation of both the active material and the electrolyte salt seems to last until the full consumption of the aqueous species, or unless a resistive LiF-rich passivation film is formed.

Having elucidated the failure mechanism of air-aged $LiFePO_4$, practical means to limit surface aging have been investigated. The preventive treatment considered calls on the deposit of a carbon coating, based on cellulose acetate precursor, which effectively circumvents iron oxidation. The effect of carbon coating on the surface reactivity of $LiFePO_4$ is however not only complex but also ambivalent. Air-aging could be prevented, and both the power capability and the cyclability improved. However, the accumulation of organic lithiated species and the probable Li consumption that results were exacerbated by the presence of the carbon coating.

The $LiFePO_4$ electrode/electrolyte interphase, although containing similar species (LiF, fluorophosphates and Li-organic) displays a drastically different behavior depending on the surface chemistry. The $LiFePO_4(OH)$ rich surface of air-aged material exacerbates the degradation of electrolyte salt in LiF, as inferred from its higher ratio detected in the interphase, and corrosive HF yielding dissolution of active material. On the other side, the carbon coating seems to favor the degradation of solvents leading to an interphase rich in lithiated organic species. Both formed interphases display clearly different properties. The resistive LiF rich interphase seems to passivate the active material particles during cycling, forming a resistive film and hindering both Li ion transfer and material corrosion while a solid electrolyte interphase allowing Li transfer and the maintaining of good electrochemical performance is formed in the case of an efficient carbon coating but seems to be lithium consuming.

## Acknowledgements

The authors wish to thank Dr. Philippe Deniard for fruitful discussion and help concerning XRD characterization.

## Appendix A. Supporting information

Supplementary data related to this article can be found at http://dx.doi.org/10.1016/j.jpowsour.2013.06.042.

## References

[1] A.K. Padhi, K.S. Nanjundaswamy, J.B. Goodenough, J. Electrochem. Soc. 144 (1997) 1188.
[2] A. Yamada, S.C. Chung, K. Hinokuma, J. Electrochem. Soc. 148 (2001) A224.

[3] C. Delacourt, P. Poizot, S. Levasseur, C. Masquelier, Electrochem. Solid-State Lett. 9 (2006) A352.
[4] B. Ellis, H.K. Wang, W.R.M. Makahnouk, L.F. Nazar, J. Mater. Chem. 17 (2007) 3248.
[5] D.H. Kim, J. Kim, Electrochem. Solid-State Lett. 9 (2006) A439.
[6] M. Armand, M. Gauthier, J.-F. Magnan, N. Ravet, World Patent WO 02/27823 A1, 2002.
[7] R. Dominko, M. Gaberscek, J. Drofenik, M. Bele, S. Pejovnik, Electrochem. Solid State Lett. 4 (2001) A187.
[8] H. Gabrisch, J.D. Wilcox, M.M. Doeff, Electrochem. Solid-State Lett. 9 (2006) A360.
[9] Y. Wang, J. Wang, J. Yang, Y. Nuli, Adv. Funct. Mater. 16 (2006) 2135.
[10] H. Huang, S.C. Yin, L.F. Nazar, Electrochem. Solid-State Lett. 4 (2001) A170.
[11] S.Y. Chung, J.T. Bloking, Y.M. Chiang, Nat. Mater. 1 (2002) 123.
[12] Z.H. Chen, J.R. Dahn, J. Electrochem. Soc. 149 (2002) A1184.
[13] D. Aurbach, M.D. Levi, E. Levi, H. Teller, B. Markovsky, G. Salitra, L. Heider, J. Electrochem. Soc. 145 (9) (1998) 3024.
[14] B.P. Abraham, R.D. Twesten, M. Balasubramanian, I. Petrov, J. McBreen, K. Amine, Electrochem. Commun. 4 (2002) 620.
[15] D. Mori, H. Kobayashi, M. Shikano, H. Nitani, H. Kageyama, S. Koike, H. Sakaebe, K. Tatsumi, J. Power Sources 189 (2009) 676.
[16] M. Koltypin, D. Aurbach, L. Nazar, B. Ellis, J. Power Sources 174 (2007) 1241.
[17] N. Dupré, J.-F. Martin, J. Oliveri, P. Soudan, D. Guyomard, A. Yamada, R. Kanno, J. Electrochem. Soc. 156 (5) (2009) C180–C185.
[18] N. Dupré, J.-F. Martin, D. Guyomard, A. Yamada, R. Kanno, J. Power Sources 189 (2009) 557.
[19] L. El Ouatani, R. Dedryvère, C. Siret, P. Piensan, D. Gonbeau, J. Electrochem. Soc. 156 (6) (2009) A468.
[20] N. Dupré, J.-F. Martin, J. Oliveri, D. Guyomard, A. Yamada, R. Kanno, Electrochem. Commun. 10 (12) (2008) 1897.
[21] C.A.J. Fisher, M. Islam, J. Mater. Chem. 18 (2008) 1209.
[22] W. Porcher, B. Lestriez, S. Jouanneau, D. Guyomard, J. Electrochem. Soc. 156 (2009) A133.
[23] L. Wang, F. Zhou, Y.S. Meng, G. Ceder, Phys. Rev. B 76 (2007) 165435.
[24] S. Hamelet, P. Gibot, M. Casas-Cabanas, D. Bonnin, C.P. Grey, J. Cabana, J.B. Leriche, J. Rodriguez-Carvajal, M. Courty, S. Levasseur, C. Masquelier, J. Mater. Chem. 19 (2009) 3979.
[25] M. Cuisinier, J.-F. Martin, R. Kanno, D. Guyomard, N. Dupré, J. Power Sources 224 (2013) 50.
[26] J.-F. Martin, A. Yamada, G. Kobayashi, S. Nishimura, R. Kanno, D. Guyomard, N. Dupré, Electrochem. Solid-State Lett. 11 (1) (2007) A12.
[27] M. Cuisinier, J.-F. Martin, N. Dupre, A. Yamada, R. Kanno, D. Guyomard, Dominique, Electrochem. Commun. 12 (2) (2010) 238.
[28] J.-F. Martin, M. Cuisinier, N. Dupré, A. Yamada, R. Kanno, D. Guyomard, J. Power Sources 196 (2011) 2155.
[29] M. Cuisinier, J.-F. Martin, N. Dupre, Ryoji Kanno, Dominique Guyomard, J. Mater. Chem. 21 (2011) 18575.
[30] A. Yamada, H. Koizumi, S.I. Nishimura, N. Sonoyama, R. Kanno, M. Yonemura, T. Nakamura, Y. Kobayashi, Nat. Mater. 5 (2006) 357.
[31] G.W. Brindley, Philosophical Magazine (Series 7) 36 (256) (1945) 347–369.
[32] N. Dupré, J.-F. Martin, D. Guyomard, A. Yamada, R. Kanno, J. Mater. Chem. 18 (2008) 4266.
[33] M. Ménétrier, C. Vaysse, L. Croguennec, C. Delmas, C. Jordy, F. Bonhomme, P. Biensan, Electrochem. Solid State Lett. 7 (6) (2004) A140.
[34] M. Cuisinier, J.F. Martin, P. Moreau, T. Epicier, R. Kanno, D. Guyomard, N. Dupré, Solid State Nucl. Magn. Reson. 42 (2012) 51.
[35] D. Massiot, http://nmr.cemhti.cnrs-orleans.fr/dmfit/.
[36] L.J.M. Davis, I. Heinmaa, B.L. Ellis, L.F. Nazar, G.R. Goward, Phys. Chem. Chem. Phys. 13 (2011) 5171.
[37] T.J. Swift, in: G.N. La Mar, W.DeW. Horrocks Jr., R.H. Holm (Eds.), NMR of Paramagnetic Materials, Academic Press, New York, 1973, p. 53.
[38] S.F. Yang, Y.N. Song, P.Y. Zavalij, M.S. Whittingham, Electrochem. Commun. 4 (2002) 239.
[39] F. Hatert, P. Schmid-Beurmann, $Fe2^{+}$ Oxidation in Triphylite $LiFePO_4$: Possible Formation of Ferrisicklerite and Heterosite, in: European Conference on Mineralogy, E. Schweizerbart Science Publishers, 2005.
[40] M. Maccario, L. Croguennec, A. Wattiaux, E. Suard, F. Le Cras, C. Delmas, Solid State Ionics 179 (2008) 2020.
[41] J.F. Martin, A. Yamada, G. Kobayashi, S.I. Nishimura, R. Kanno, D. Guyomard, N. Dupré, Electrochem. Solid State Lett. 11 (2008) A12.
[42] G. Kobayashi, S. Nishimura, M. Park, R. Kanno, M. Yashima, T. Ida, A. Yamada, Adv. Funct. Mater. 19 (2009) 395.
[43] S.D. Berger, D.R. McKenzie, P.J. Martin, Philos. Mag. Lett. 57 (1988) 285.
[44] J.J. Cuomo, J.P. Doyle, J. Bruley, J.C. Liu, Appl. Phys. Lett. 58 (1991) 466.
[45] P.J. Fallon, V.S. Veerasamy, C.A. Davis, J. Robertson, G. Amaratunga, W. Milne, J. Koskinen, Phys. Rev. B 48 (1993) 4777.
[46] J. Bruley, D.B. Williams, J.J. Cuomo, J. Microsc. – Oxford 180 (1995) 22.
[47] J. Bruley, P. Madarson, J.C. Liu, Nucl. Instrum. Methods Phys. Res. B 45 (1990) 618421.
[48] J.G. Thevenin, R.H. Muller, J. Electrochem. Soc. 134 (1987) 273.
[49] C.P. Grey, N. Dupre, Chem. Rev. 104 (2004) 4493.
[50] N. Dupré, J.-F. Martin, J. Degryse, V. Fernandez, P. Soudan, D. Guyomard, J. Power Sources 195 (21) (2010) 7415.
[51] K. Edström, T. Gustafsson, J.O. Thomas, Electrochim. Acta 50 (2004) 397.
[52] A. Nyten, M. Stjerndahl, H. Rensmo, H. Siegbahn, M. Armand, T. Gustafsson, K. Edstrom, J.O. Thomas, J. Mater. Chem. 16 (2006) 3483.
[53] V. Eshkenazi, E. Peled, L. Burstein, D. Golodnitsky, Solid State Ionics 170 (2004) 83.
[54] R. Dedryvère, S. Laruelle, S. Grugeon, L. Gireaud, J.M. Tarascon, D. Gonbeau, J. Electrochem. Soc. 152 (2005) A689.
[55] D. Aurbach, I. Weissman, A. Schechter, Langmuir 12 (1996) 3991.
[56] B. Ravdel, K.M. Abraham, R. Gitzendanner, J. DiCarlo, B. Lucht, C. Campion, J. Power Sources 119–121 (2003) 805.
[57] T. Kawamura, S. Okada, J.I. Yamaki, J. Power Sources 156 (2006) 547.
[58] H. Yang, G.V. Zhuang, P.N. Ross Jr., J. Power Sources 161 (2006) 573.
[59] J. Barker, M.Y. Saidi, J.L. Swoyer, J. Electrochem. Soc. 150 (2003) A1394.